Soliton dynamics of ring quantum cascade lasers with injected signal

Research article

Franco Prati*, Massimo Brambilla, Marco Piccardo, Lorenzo Luigi Columbo, Carlo Silvestri, Mariangela Gioannini, Alessandra Gatti, Luigi A. Lugiato and Federico Capasso

Soliton dynamics of ring quantum cascade lasers with injected signal

https://doi.org/10.1515/nanoph-2020-0409
Received July 21, 2020; accepted September 21, 2020; published online October 14, 2020

Abstract: Nonlinear interactions in many physical systems lead to symmetry breaking phenomena in which an initial spatially homogeneous stationary solution becomes modulated. Modulation instabilities have been widely studied since the 1960s in different branches of nonlinear physics. In optics, they may result in the formation of optical solitons, localized structures that maintain their shape as they propagate, which have been investigated in systems ranging from optical fibres to passive microresonators. Recently, a generalized version of the Lugiato–Lefever equation predicted their existence in ring quantum cascade lasers with an external driving field, a configuration that enables the bistability mechanism at the basis of the formation of optical solitons. Here, we consider this driven emitter and extensively study the structures emerging therein. The most promising regimes for localized structure formation are assessed by means of a linear stability analysis of the homogeneous stationary solution (or continuous-wave solution). In particular, we show the existence of phase solitons – chiral structures excited by phase jumps in the cavity – and cavity solitons. The latter can be deterministically excited by means of writing pulses and manipulated by the application of intensity gradients, making them promising as frequency combs (in the spectral domain) or reconfigurable bit sequences that can encode information inside the ring cavity.

Keywords: frequency combs; quantum cascade lasers; solitons.

***Corresponding author: Franco Prati**, Dipartimento di Scienza e Alta Tecnologia, Università dell'Insubria, Via Valleggio 11, 22100 Como, Italy, E-mail: franco.prati@uninsubria.it
Massimo Brambilla, Dipartimento di Fisica Interateneo and CNR-IFN, Università e Politecnico di Bari, Via Amendola 173, 70123 Bari, Italy
Marco Piccardo, Center for Nano Science and Technology, Fondazione Istituto Italiano di Tecnologia, Via Giovanni Pascoli 70, 20133 Milano, Italy; Harvard John A. Paulson School of Engineering and Applied Sciences, Harvard University, Cambridge, MA, USA
Lorenzo Luigi Columbo, Carlo Silvestri and Mariangela Gioannini, Dipartimento di Elettronica e Telecomunicazioni, Politecnico di Torino, Corso Duca degli Abruzzi 24, 10129 Torino, Italy. https://orcid.org/0000-0002-6566-9763 (L.L. Columbo)
Alessandra Gatti, Dipartimento di Scienza e Alta Tecnologia, Università dell'Insubria, Via Valleggio 11, 22100 Como, Italy; Istituto di Fotonica e Nanotecnologie, IFN-CNR Piazza Leonardo da Vinci 32, Milano, Italy
Luigi A. Lugiato, Dipartimento di Scienza e Alta Tecnologia, Università dell'Insubria, Via Valleggio 11, 22100 Como, Italy
Federico Capasso, Harvard John A. Paulson School of Engineering and Applied Sciences, Harvard University, Cambridge, MA, USA

1 Introduction

Optical frequency combs [1, 2] have revolutionized the field of optics and optoelectronics, both from the fundamental and from the application standpoint. The realization, nearly 13 years ago, of frequency combs in high-Q monolithic microresonators filled with Kerr media [3] raised an enormous attention because of its potential for miniaturization and chip-scale photonic integration, and stimulated a great deal of activities [4–6]. More recently, another system relevant for photonic integration, namely the quantum cascade laser (QCL) emerged as a source of frequency combs [7–12]. Close to its lasing threshold, the dynamics of a QCL is governed by a cubic nonlinearity similar to the one of Kerr cavities. On the other hand, unlike Kerr cavities which are passive, in the QCL the medium is active, i.e. with a population inversion.

Frequency combs in active and passive systems have been so far studied in distinct frameworks, and only recently a definite connection emerged [13, 14]. In particular, in the study by Columbo et al. [14], the treatment of frequency combs in passive and active systems was unified by formulating a generalized version of the Lugiato–Lefever equation (LLE) [15, 16]. For passive systems, this generalized model reduces to the LLE of Lugiato and Lefever [15], largely used to describe frequency combs in Kerr ring microresonators [4]. In the active case, under the approximations of fast material dynamics and near-threshold

operation, it becomes the complex Ginzburg–Landau equation (CGLE) derived in the study by Piccardo et al. [13] for a free-running ring QCL, on the one hand, and the cubic equation formulated in the study by Lugiato et al. [16] for a two-level ring laser, on the other.

A relevant point is that while in the passive case frequency combs need an external field providing the necessary energy intake, in active systems like the QCL frequency combs are generated in a free-running setup [7, 9–13]. The generalized LLE also contemplates a novel configuration, to our knowledge never analysed before, in which a ring QCL is driven by an external coherent field (QCL with injected signal). This setup is of special interest because it introduces two new control parameters, namely the intensity and the frequency of the injected signal, which creates conditions favourable for the generation and control of temporal solitons [17], relevant for new applications in integrated comb technology such as metrology and spectroscopy. Indeed a first analysis of this model [14] demonstrated the emergence of temporal solitons in ring QCL with injected signal, and the possibility of addressing them by means of external pulses.

In the present work, we perform a more extensive analysis, which provides novel insights in the rich dynamical scenery of the injected ring QCL. The linear stability analysis of the *S*-shaped homogeneous stationary solution (HSS) allows establishing the conditions for the stability of the lower and upper branch by associating the bifurcation point of the lower branch with a plane wave Hopf instability and that of the upper branch with a modulational instability. We show that when the upper branch is stable and the lower branch is unstable, the system supports localized structures characterized by phase jumps equal to (a multiple of) 2π, named phase solitons (PSs), whereas in the opposite situation, when the upper branch is unstable and the lower branch is stable, the localized structures are bright solitons on a homogeneous background, similar to those observed in Kerr microresonators [18]. Focussing on cavity solitons (CSs), we study the basic properties, fundamental for their exploitation as elements for optical information encoding. Namely, we show independent switch-on of CSs, by means of suitable address pulses superimposed to the constant driving field. We determine the optimal amplitude and duration of such pulses for the creation of a single soliton and the minimum distance at which pairs of solitons can be created independently. The possibility of controlling the solitons by means of appropriate gradients in the driving field is verified, thus assessing the CSs as plastic information units which can be deterministically drifted/relocated across the cavity field profile.

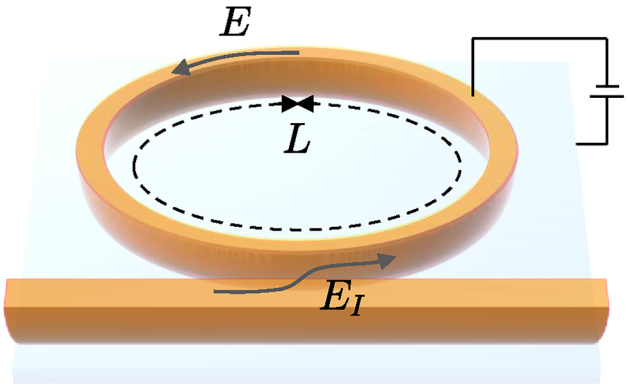

Figure 1: Schematic of a ring quantum cascade laser (QCL) under electrical bias with an injected optical signal. The ring cavity has a length L and the intracavity field is E. The external field E_I is injected into the QCL from a straight waveguide.

2 The model

A possible realization of the system analysed in this work is schematically shown in Figure 1: we consider a ring QCL in a ridge-waveguide geometry, similar to the one used in the study by Piccardo et al. [13], but coupled to a straight waveguide by which a coherent field can be injected into the ring with round-trip cavity length L.

We showed in the Supplementary material of the study by Columbo et al. [14] that a driven QCL can be suitably described by the generalized LLE

$$\tau_p \frac{\partial E}{\partial t} = E_I - (1 + i\theta_0)E + (1 - i\Delta)\left(\mu - |E|^2\right)E + (d_R + id_I)\frac{\partial^2 E}{\partial z^2}, \tag{1}$$

where t is the time variable and z the longitudinal coordinate along the ring cavity in a reference frame moving at the phase velocity $\tilde{c} = c/n_h$, n_h being the refractive index of the host material. E and E_I are the envelopes of the intracavity electric field and of the external field injected into the cavity, respectively, normalized as in the study by Columbo et al. [14]. When referred to a QCL close to its lasing threshold, the parameters appearing in the equation are as follows:

- τ_p is the damping time of the cavity field (typical values are some tens of ps);
- μ is the pump parameter, such that the laser threshold is at $\mu = \mu_{thr} = 1$;
- $\Delta = \alpha + \beta$, where α is the so-called linewidth enhancement factor (LEF) [19] and β is the Kerr nonlinear coefficient of the host medium, which in a QCL is normally small;
- $\theta_0 = (\omega_c - \omega_0)\tau_p - \mu\beta$, is a detuning parameter, where ω_c is the cavity frequency closest to the reference

frequency ω_0 of the injected field. The term $\mu\beta$ arises from the specific form chosen for the generalized LLE in [14], but it does not contribute to the equation because it cancels out with another identical term;

- $d_R = (\check{c}\tau_d)^2/(1+\alpha^2)$ represents a diffusion term, where τ_d is the dipole dephasing time. $\sqrt{d_R}$ has the dimension of a length, and defines the spatial length scale. By using typical values for a QCL [13] ($\tau_d = 60$ fs, $n_h = 3.3$, $\alpha \simeq 1.9$), we get $\sqrt{d_R} \simeq 2.5\,\mu$m.
- $d_I = d_R(\alpha + \zeta)$ represents a second order dispersion term, where $\zeta = -(1+\alpha^2)\check{c}\tau_p k''/(2\tau_d^2)$, and k'' is the group velocity dispersion (GVD) coefficient of the host medium. Notice that $\zeta > 0$ in the case of anomalous dispersion. Assuming $\tau_p = 50$ ps and $k'' = -300$ fs^{2}mm^{-1} [14] we have $\zeta \simeq 0.9$. Notice however that the GVD can be engineered to take much smaller values, such that $\zeta \simeq 0$.

We note that in the study by Columbo et al. [14], the third term at the r.h.s. of the equation was written as $\mu(1-i\Delta)(1-|E|^2)E$ rather than $(1-i\Delta)(\mu-|E|^2)E$, but the two forms are equivalent in the limit of a laser very close to threshold where $\mu \approx 1$ and $|E|^2 \ll 1$ is on the same order as $|\mu-1|$.

Next, we introduce a small (but not necessarily infinitesimal) parameter $r = \mu - \mu_{thr}$ measuring the distance from the laser threshold. To have finite quantities appearing in the equation, and to minimize the number of parameters, we introduce the following scaling:

$$\tau = t|r|/\tau_p, \quad \eta = z\sqrt{|r|/d_R}, \quad F = E/\sqrt{|r|}, \quad F_I = E_I/|r|^{3/2}, \quad (2)$$

Eq. (1) then takes the form of a forced complex Ginzburg–Landau equation [20]

$$\frac{\partial F(\tau,\eta)}{\partial \tau} = F_I + \gamma(1-i\theta)F - (1-i\Delta)|F|^2F + (1+iG)\frac{\partial^2 F}{\partial \eta^2}, \quad (3)$$

where

$$\gamma = r/|r|, \quad \theta = [(\omega_c-\omega_0)\tau_p+\alpha]/r+\alpha, \quad G = d_I/d_R = \alpha+\zeta. \quad (4)$$

In this work, we shall focus on the above threshold case, and fix $\gamma = 1$.

An important point to remark is that, because F_I and F need to be on the same order of magnitude, a consequence of the scaling (2) is that E_I is smaller than E by a factor $|r| \ll 1$; this implies that the system can be operated with an injected field of small intensity, which is particularly convenient when the laser cavity is ring-shaped. A second remark concerns the relevant temporal and spatial scales of variation of the intracavity field. These are established by $\tau_p/|r|$ (time) and $\sqrt{d_R/|r|}$ (longitudinal coordinate) and depend on the distance from threshold, getting larger and larger as threshold is approached, as typical of phase transitions.

Besides the ring geometry considered here, a connection between QCLs and the LLE was also established recently in the case of Fabry–Perot devices [21].

3 Homogeneous stationary solution and its stability

As typical of forced cubic equations, the HSS of Eq. (3) may show a bistable behaviour. This in turn creates conditions favourable to the emergence of localized structures, as e.g. a modulation instability appearing in the upper branch in the presence of a stable lower branch [22]. The choice of parameters for the simulations presented in Section 4 will thus be guided by the results of the stability analysis presented in this section.

By introducing the quantities $Y = F_I^2$ and $X = |F|^2$, proportional to the input and output intensity, respectively, the homogeneous and stationary solution of Eq. (3) has the form

$$Y = X\left[(1-X)^2 + (\theta-\Delta X)^2\right]. \quad (5)$$

When plotting X versus Y, the curve is S-shaped provided that

$$1 + \Delta\theta > \sqrt{3}|\Delta - \theta|. \quad (6)$$

An example of such stationary curve is shown in Figure 2 (see also Figure 5). The blue symbols in this figure are

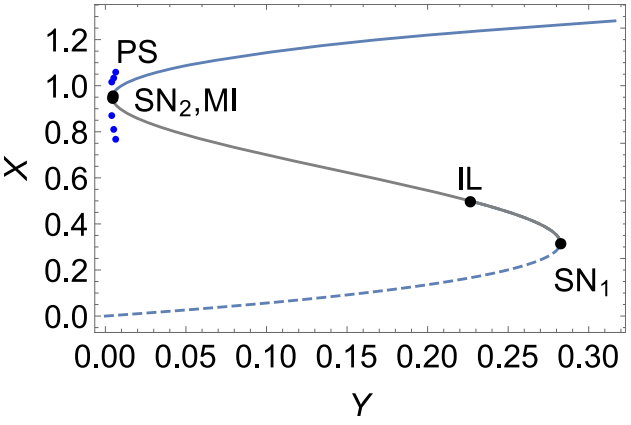

Figure 2: Stationary homogeneous solution of Eq. (3), where the solid and dashed blue lines denote stable and unstable configurations. The blue symbols correspond to a phase soliton branch from numerical simulations of Eq. (3) with $\eta_{max} = 200$ (the symbols indicate the maximum and minimum intensity). $\Delta = G = 1.1$, $\theta = 1$ (point **a** of Figure 3).

related to the PSs that will be discussed in the following Section 4. SN_1 and SN_2 denote the lower and upper turning points of the *S*-shaped curve (the origin of the naming is that in the single-mode limit these points are related to a saddle-node bifurcation). The grey portion of the curve between the points, having a negative slope, is not accessible. If $\theta = \Delta$ the upper turning point SN_2 touches the X axis at $X = 1$.

3.1 Hopf instability

In Figure 2, IL denotes the so-called injection locking point, below which a Hopf instability takes place. Irrespective of the other parameters, the solution (5) is temporally unstable for $X < X_{IL} = 0.5$. The presence of such an injection locking point is characteristic of a laser above threshold when a slightly detuned external field is injected. Then, only for a sufficiently high injection amplitude the laser locks to the external field [23]. In class A lasers, as the QCL, the injection locking occurs at an output intensity $|E|^2 = \sqrt{\mu_{\rm thr}}(\sqrt{\mu} - \sqrt{\mu_{\rm thr}})$ [see Eq. (25.3) of [24]]. For our scaled quantities $\mu_{\rm thr} = 1$, $\mu = 1 + r$, and $X = |E|^2/r$ (see Eq. (2)), so that $X_{IL} = (\sqrt{1+r} - 1)/r \to 0.5$ in the limit $r \ll 1$.

In the bistable case, it is important to determine the position of the injection point with respect to the turning points, in order to assess the existence of a stable portion of the lower branch of the stationary curve. To this end, there

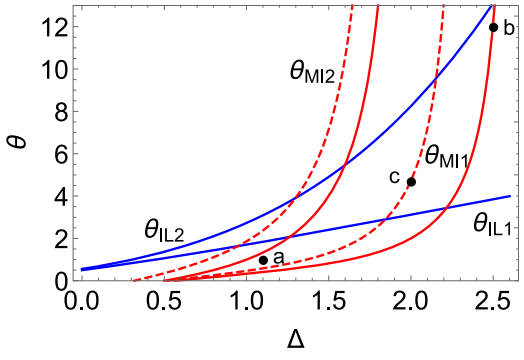

Figure 3: Critical values of the parameter θ as functions of Δ for the Hopf instability (blue) and for the modulational instability (red), for $G = \Delta$ (solid red lines) and $G = \Delta + 1$ (dashed red lines). The points marked as **a**, **b**, and **c** correspond to the parameters used in the numerical simulations, with $G = \Delta$ for **a** and **b**, and $G = \Delta + 1$ for **c**. In the region below the blue curves (point **a**), the lower branch is unstable because it is below the injection locking point. In the region between them (points **b** and **c**), the lower branch of the *S* has a stable portion. In the region between the red curves, the bifurcation point MI of the modulational instability is placed in the upper branch between the two turning points.

exist two critical values of the parameter θ, that we denote by $\theta_{\rm IL1}(\Delta)$ and $\theta_{\rm IL2}(\Delta)$, given by Eq. (S6) and Eq. (S7) of the Supplementary material, respectively, and plotted by the blue curves in Figure 3, such that:

- For $\theta < \theta_{\rm IL1}(\Delta)$ the injection locking point is always above the lower turning point SN_1. In this case, the whole lower branch of the *S*-shaped stationary curve is unstable, as in the example of Figure 2.
- For $\theta_{\rm IL1}(\Delta) < \theta < \theta_{\rm IL2}(\Delta)$, the injection locking point is below SN_1, but still in the bistable part of the curve, so that the lower branch of the curve has an unstable and a stable portion between the two turning points, as in Figure S2.
- For $\theta > \theta_{\rm IL2}(\Delta)$, the injection point is at the left of the upper turning point SN_2, and the Hopf instability does not affect the bistability region. In this case, the whole lower branch between the turning points is stable.

In the example of Figure 5, the lower branch of the curve is almost entirely stable, because θ is very close to $\theta_{\rm IL2}$.

3.2 Modulational instability

The upper branch of the stationary curve is affected by a modulational instability from the left turning point SN_2 up to the bifurcation point MI. Again, it is important to determine the position of the MI point with respect to the turning points.

The position of the MI point on the stationary curve now depends on the whole triplet of parameters Δ, G and θ. As for the Hopf instability, we can introduce two critical values of θ, that we denote by $\theta_{\rm MI1}(\Delta, G)$ and $\theta_{\rm MI2}(\Delta, G)$. Their explicit expressions are given by Eq. (S10) and Eq. (S8), respectively, whereas examples are provided by the red curves in Figure 3.

- For $\theta < \theta_{\rm MI1}(\Delta, G)$, the whole upper branch between the two turning points is modulationally unstable.
- For $\theta_{\rm MI1}(\Delta, G) < \theta < \theta_{\rm MI2}(\Delta, G)$, the MI point is in the upper branch of the curve between the turning points, so that only a portion of the upper branch is modulationally unstable.
- For $\theta = \theta_{\rm MI2}(\Delta, G)$, the modulational instability disappears, while it appears again at higher values of θ.

Figure 3 shows the critical values of θ as functions of Δ both for the Hopf instability (blue lines) and for the MI (red lines). In the figure are also shown the points which will be numerically studied in the rest of the article. Point **a** provides the ideal conditions for the emergence of the PSs that will be discussed in Section 4.1; point **b** has instead the proper conditions for the emergence of the CSs with stable

background that will be analysed in Section 4.2, whereas for the parameters of point **c,** the background of the CSs can be stable or unstable depending on the amplitude of the driving field. That case has been already presented in the study by Columbo et al. [14]; here, we provide further details and results in Section 5 and in the Supplementary material.

4 Optical solitons

In this section, we present results of numerical simulations of Eq. (3). The scaled cavity coordinate runs from 0 to $\eta_{\max} = L\sqrt{|r|/d_R}$, where L is the real cavity length. In the figures, the cavity coordinate is shown as $\eta/\eta_{\max} = z/L$. The temporal coordinate is shown as the scaled time $\tau = tr/\tau_p$ (Eq. (2)). The connection with physical quantities, as the cavity roundtrip time, then depends on the distance from threshold. By assuming, e.g. a loss coefficient of the cavity ≃0.7 (including both the external coupling and distributed losses) [14], the photon lifetime is $\tau_p \simeq L/(0.7\tilde{c})$, so that one scaled time unit corresponds to ~1.43/r roundtrips, that is 14.3 roundtrips for e.g. a laser 10% above threshold.

4.1 Phase solitons

In the first simulation, we consider point **a** of Figure 3, by setting $\Delta = G = 1.1$, a value which is realistic for a QCL (LEF = 1.1 and negligible GVD), and $\theta = 1$. This value of θ is smaller than θ_{IL1}, so that the lower branch is entirely unstable, whereas it is close to θ_{MI2}, and the point MI is very close to SN_2, so that the upper branch is almost entirely stable. For input intensities close enough to SN_2, these conditions are favourable for observing excitable pulses in the single mode limit, and localized structures associated with a phase kink in the multimode regime [25, 26]. The latter can be excited taking as initial condition the stable state of the upper branch to which a phase kink is superimposed, i.e. a phase profile along z with a sharp jump equal to $2l\pi$, where l is an integer number. In this way, the boundary condition on the phase imposed by the injected field is still obeyed but, as light propagates along the cavity, the phasor associated with the complex electric field rotates l times around the origin. Because the dynamics of the phase is coupled to that of the amplitude, the length of this phasor varies accordingly, letting the field intensity profile to exhibit a local modulation in correspondence with the phase jump. This kind of structure is called phase soliton (PS) because its dynamics is dominated by the phase, and it is chiral in nature, having positive or negative chiral charge depending on the sign of the integer l. Here we consider only the PS with chiral charge equal to 1.

With the parameters of Figure 2, PSs are stable in the interval $0.0043 \le Y \le 0.0058$. Figure 4(a,b) illustrates the PS with $Y = 0.005$. The upper plot in panel (a) shows the space-time evolution of the emitted intensity. Note that the PS trace is slanted to the left, which means that the PS travels along the cavity at a speed slightly smaller than $\tilde{c}$. The PS accumulates a delay of one roundtrip time τ_r in about 600 time units. Assuming as aforementioned that 1 unit in τ corresponds to 1.43/r roundtrip times, the speed of the PS is $V_{\mathrm{PS}} = \tilde{c}/[1 + r/(1.43 \times 600)] \simeq \tilde{c}\,(1 - 1.17 \times 10^{-4})$ for a laser 10% above threshold. The bottom plot shows the field optical spectrum at the end of simulation, which for a PS is an asymmetric frequency comb. The first two plots from the top in panel b show the intensity and phase profiles along the cavity at the last round trip. The phase displays a negative jump of 2π in correspondence with the PS. A modulation of the intensity, consisting in a maximum followed by a minimum, is associated with the phase jump. The bottom graph in panel b shows the trajectory described by the tip of the electric field phasor in the complex plane. The trajectory is close to a circle, drawn in green in the bottom panel of Figure 4(b), indicating that the dynamics is an almost pure phase dynamics, but nevertheless the length of the phasor is not constant and this causes the modulation of the intensity.

In this figure, we show the PS with positive chiral charge. The PS with negative chiral charge is also stable. For that PS, the trace in the space-time plot is slanted to the right (the PS travels faster than $\tilde{c}$), in the intensity profile the minimum precedes the maximum, the phase jump is positive, the spectrum is identical to the previous one but with $n \to -n$, and the electric field vector rotates in the complex plane in the opposite direction.

PSs in a forced CGLE, whose existence is made possible by the presence of an unstable focus close to the origin of the complex plane, were predicted in the study by Chaté, Pikovsky and Rudzick [25] and observed in the study by Gustave et al. [26] in a driven semiconductor laser. In the study by Gustave et al. [26], however, the active medium was an interband semiconductor with a slow recovery time of gain (~1 ns) and just one sign of the chirality [27, 28] was observed because of the inertia of the medium. This feature cannot be captured by the forced CGLE alone, which in fact was coupled with a dynamical equation for the gain in previous studies [26–28]. In the aforementioned simulations, PSs are found stable with both signs of the chirality in a driven QCL, based on our model where, although, the adiabatic elimination of all material variables is a

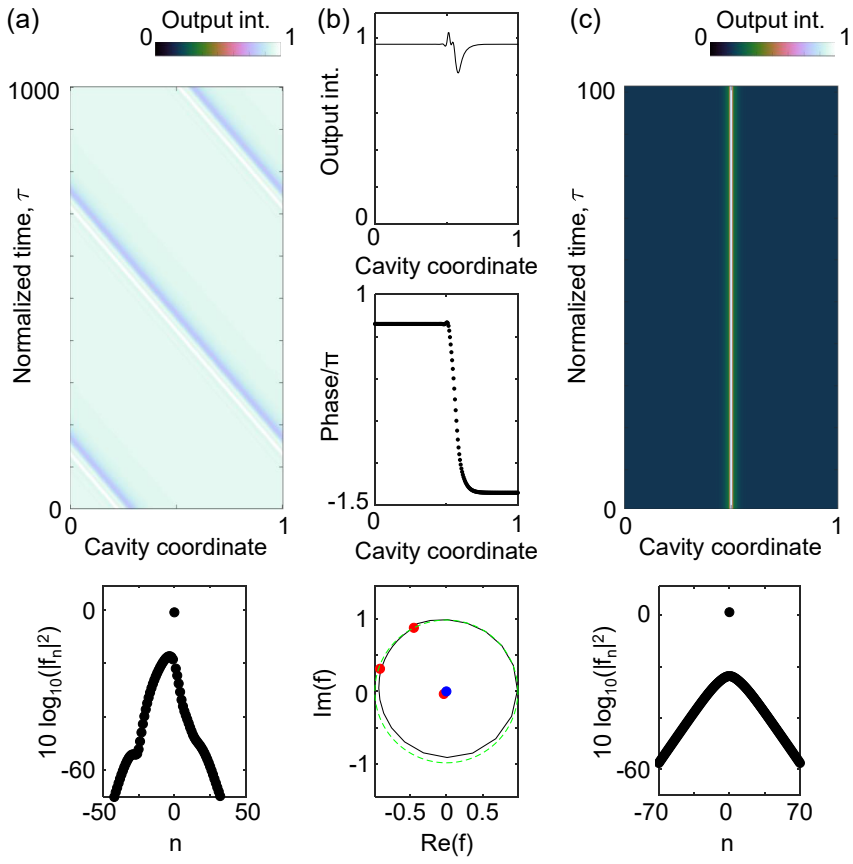

Figure 4: (a) Phase soliton for the same parameters of Figure 2 and $Y = 0.005$. The upper plot is the space-time evolution of the intensity, whereas the bottom plot is the optical spectrum at the last roundtrip, n being the index of the empty cavity mode of complex amplitude f_n. (b) From top to bottom: field intensity along the cavity at the end of simulation; corresponding phase profile; trajectory described by the tip of the electric field phasor in the complex plane, where the red symbols are the three stationary states corresponding to $Y = 0.005$, whereas the blue one shows the origin. (c) Cavity soliton for the same parameters of Figure 5 and $Y = 100$. The upper and bottom panels show the space-time evolution and the optical spectrum at the last roundtrip, respectively.

background assumption. To substantiate a prediction for stable solitons of either charge in such a device, a more complete analysis based on a full set of effective semiconductor Maxwell–Bloch equations [14] with the appropriate medium temporal timescales will be needed.

4.2 Cavity solitons

In the second simulation, we consider point **b** of Figure 3, by setting $\Delta = G = 2.5$ and $\theta = 12$. Such a value of Δ (and hence of the LEF) is probably a bit higher than the typical one for a QCL [13], but it allows obtaining in the system stable stationary temporal solitons, also called cavity solitons (CSs), for a large interval of the input intensity. For these values of the parameters, θ is close to both θ_{IL2} and θ_{MI1}, which means that in the region between the two turning points, the lower branch is almost entirely stable and the upper branch is almost entirely unstable. These are the best conditions to find stable stationary CSs [24, 29].

Figure 5 indeed shows branches of Turing rolls and CSs as defined in the study by Columbo et al. [14] emerging in the upper branch of the stationary homogeneous solution. If we move on the upper branch from the right to the left crossing the bifurcation point MI, we observe the onset of Turing rolls, whose maximum and minimum intensity are shown by the red symbols in Figure 5. At $Y = 82$, the Turing pattern becomes unstable and one or more CSs emerge from it. The blue symbols indicate the maximum intensity of the CSs along their branch. Figure 4(c) shows a CS at steady state for $Y = 100$.

In Figure 3, the curves θ_{IL1} and θ_{MI1} for $G = \Delta$ (solid line) intersect at a point whose abscissa can be calculated analytically and it is $\Delta = (4 + \sqrt{7})/3 \simeq 2.125$. For smaller Δ, if Y_{MI} coincides or is close to Y_{SN_1} in such a way that the upper branch is modulationally unstable between the two turning points, the lower branch is entirely unstable and no stable stationary CSs exist. The picture changes if we allow G to be different from, and in particular larger than, Δ, i.e. if $G = \Delta + \zeta$ with $\zeta > 0$, which means that GVD is not negligible and dispersion is anomalous. In Figure 3, the two dashed red curves have been obtained setting $G = \Delta + 1$. They are displaced to the left with respect to the solid curves obtained with $G = \Delta$ and now the curve θ_{IL1} intersects the curve θ_{MI1} at $\Delta \simeq 1.843$. This means that if we set for instance $\Delta = 2$ and $\theta = 4.7$ (point **c** of Figure 3), we have $Y_{MI} \simeq Y_{SN1}$ and yet a

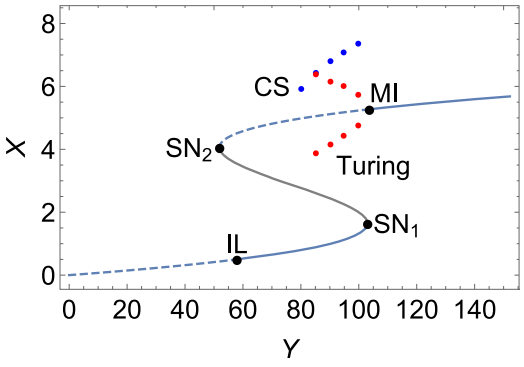

Figure 5: Stationary homogeneous solution (solid and dashed lines), cavity soliton branch (blue symbols), and Turing pattern branch (red symbols) for Eq. (3). $\Delta = 2.5$, $G = 2.5$, $\theta = 12$ (point **b** of Figure 3), and $\eta_{max} = 100$.

part of the lower branch from MI to SN_1 is stable so that stable stationary CSs may exist. For what concerns Turing patterns and CSs this set of parameters was extensively studied by Columbo et al. [14] and the main results are recalled in the Supplementary material (Figure S2). Here instead, in Section 5, we focus on the process of writing the CSs, their interaction and on how they can be manipulated by means of spatial modulations in the external field or in the bias current.

5 Cavity soliton encoding and interaction

CSs exhibit a remarkable potential for application in two ways. In the temporal domain, we can regard them as self-confined intensity pulses which, as shown by Columbo et al. [14], can not only be driven by an external continuous-wave field but also excited in arbitrary positions inside the laser cavity by the injection of optical pulses. A collection of independent CSs can thus be encoded in the cavity and associated with a bit sequence; as the CSs collection impinges on the output mirror each round-trip, a bit train is emitted through the output facet. The ring thus acts as a buffer, which can be swiftly reset and rewritten and wherein the solitons can also undergo manipulation by means of external field tailoring, as it will be treated in the following.

In the spectral domain, CSs are associated with the onset of an optical frequency comb (see Figure 2(g) in the study by Columbo et al. [14]) so that the possibility to turn multiple CSs on and to control their relative distance provides a unique way to modify in real time the spectrum shape and the frequency sets appearing in the emitted spectrum.

5.1 Switching

An especially interesting feature for any multistable, localized structure such as the CS is the possibility to be deterministically excited at any location of the extended system by means of some external control parameter. In the case of an active optical system (a laser or an amplifier), most often this “encoding channel” is a coherent external field or an incoherent pump (a bias current, in the specific case of a semiconductor laser). In our injected laser layout, we add to the homogeneous component E_I in Eq. (3) suitably tailored pulses, by intensity, duration, and delay (in case multiple CSs switching is required).

The first issue addressed here is thus the relation between the pulse magnitude and the duration of the injection to observe the formation of a stable CS. To this purpose, we modified the input field term in numerically solving Eq. (3); we adopted the form

$$\overline{F}_I(\tau,\eta) = F_I + \epsilon\,\mathrm{sech}\left[(\eta-\eta_0)w/L\right]^8 \prod(\tau/T). \qquad (7)$$

where $\prod(x)$ is the rectangular function, equal to 1 for $0 < x < 1$, and to 0 elsewhere, T is the pulse duration, η_0 is the position of the pulse inside the cavity, w/L is its width scaled to the cavity length and ϵ is the magnitude of the pulse. The $\mathrm{sech}(x)^8$ choice ensures a steep raise/drop of the pulse. In our simulations, the pulse width was taken equal to the CS full width half maximum and its location at $\eta_0/\eta_{max} = 0.5$ was never changed.

We considered two representative cases corresponding to the parametric regime of Figure S2 in the Supplementary material: the first at $Y = 7$ where the CS sits on a stable homogeneous background and the second at $Y = 6.6$ where the background is irregular but the CS is still stable although subjected to jitters (see also [14]). In the first case, when the pulse is too weak or the injection time too short, an intensity peak locally appears at the injection location but it dies rapidly away as the system returns to the HSS, emitting what could conceivably be dispersive waves [30] that ring off on a long timescale, compared with the frustrated CS decay rate (see bottom plot of Figure 6(a)). When the required magnitude and duration are met, a CS appears and rapidly becomes the stationary structure already studied by Columbo et al. [14] (Figure 6(b)). The peak intensity evolution vs. time shown in the bottom plot of Figure 6(b) evidences a latency around $X = 1.5$ as if realizing a metastable structure of intermediate intensity before reaching the CS intensity at $X = 3.7$. We remark that this is consistent with the studies performed on transverse 2D CSs [31] and pointed to the existence of an unstable CS branch bifurcating subcritically from the MI threshold which acts

as a separatrix between the HSS branch and the stable CS branch coexisting with it. In this viewframe, a localized pulse causes the local field to grow from the HSS value; if the injection is large enough and it lasts long enough to draw the local field beyond the separatrix, the system locally reaches the CS branch and the structure is formed at regime. While a proper proof that this scenery occurs in our injected laser would require analyses of the stable and unstable parts of the CS branch, and of the CS eigenspectrum, we can suggest that the latency on the intermediate state, may flag the persistence of the system state around the attraction basin of the unstable CS before being finally attracted by the absolute stable solution. Note that in Figure 6(b), the plateau reached by the frustrated CS lies below $X = 1.5$ which seems to separate simulations of frustrated switch-on from successful ones. As the pulse duration grows larger than the critical value reported previously ($T = 0.89$), the CS transient, i.e. the CS switch-up time, becomes shorter and settles at about 3. For a resonator with τ_p on the order of some tens of ps and 10% above threshold, it means that the switching time is on the order of some ns.

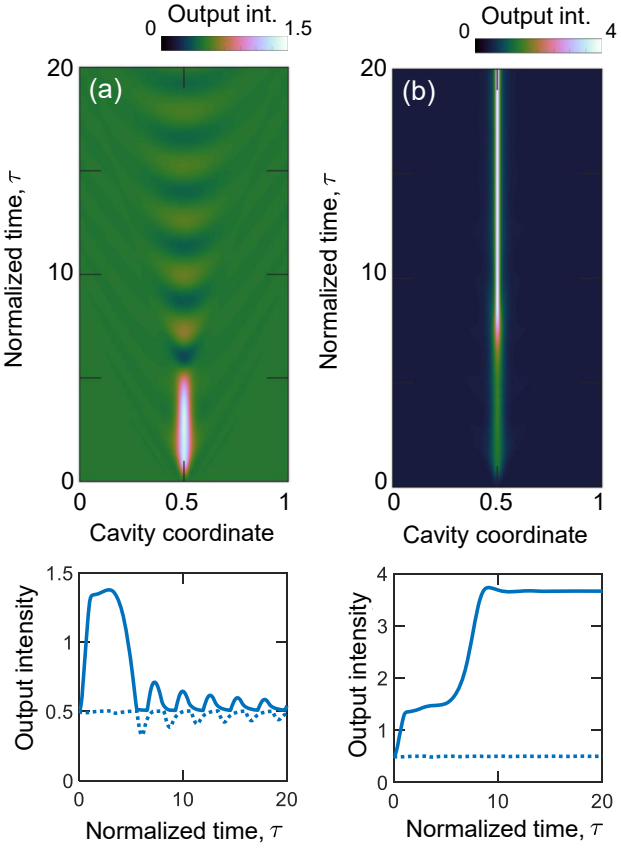

Figure 6: $Y = 7$. (a) Frustrated cavity soliton (CS) switching. The pulse width and duration are $\epsilon = 0.5$ and $T = 0.88$, respectively. The local field maximum does not evolve to a stable CS and rings off in rippling waves. (b) CS switch-on. Here the pulse width and duration are $\epsilon = 0.5$ and $T = 0.89$ where T is just above the critical switch-on value. Space-time diagrams (upper panels) and output intensity vs time (bottom panels) are reported in both cases.

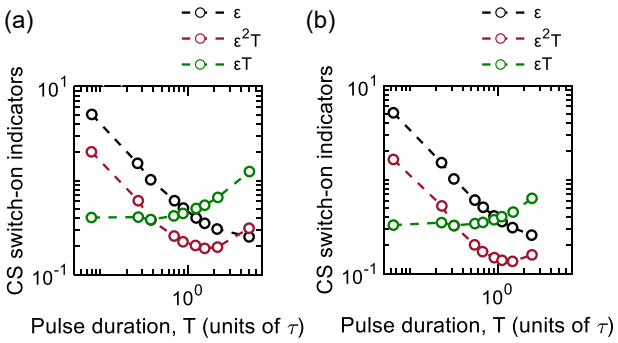

Figure 7: The critical values of a few indicators which correspond to successful cavity soliton (CS) switch-on for (a) $Y = 7$; (b) $Y = 6.6$.

Systematic simulations in both study cases $Y = 7$ and $Y = 6.6$ for various pulse amplitude ϵ and duration T allow estimating the critical values for the pair and plot the relative curve. In agreement with Brambilla, Lugiato and Stefani [32], the product ϵT is approximately constant, as compared with e.g. the quantity $\epsilon^2 T$, proportional to energy as Figure 7 shows for both cases inspected, revealing small differences between the two, meaning that the switch-on process is not strongly influenced by the background behaviour. The major departures from constant ϵT occur for small injection values, when longer and longer injection times are required. In fact, for $\epsilon < 0.25$ no CS could be switched on, regardless the injection time. This suggests that the CS switch-on is a coherent phenomenon, similar to the onset of the self-induced-transparency solitons of the Sine–Gordon equation [24]. Finally, we observed that when the pulse intensity increases well beyond the critical value, the switch-on time decreases and tends to settle to about one roundtrip time.

5.2 Interaction

To determine the bit density which a cavity can sustain by allocating a certain number of CSs, it is necessary to estimate their interaction distance, defined here as the minimum distance two CSs can be excited at and reach a regime where no CS merging, or other forms of permanent pattern deformation, can be observed. We remark that, together with the CS transient time and the reset time required to start CS encoding anew, this figure contributes to the determination of the bit flux sustained by the device.

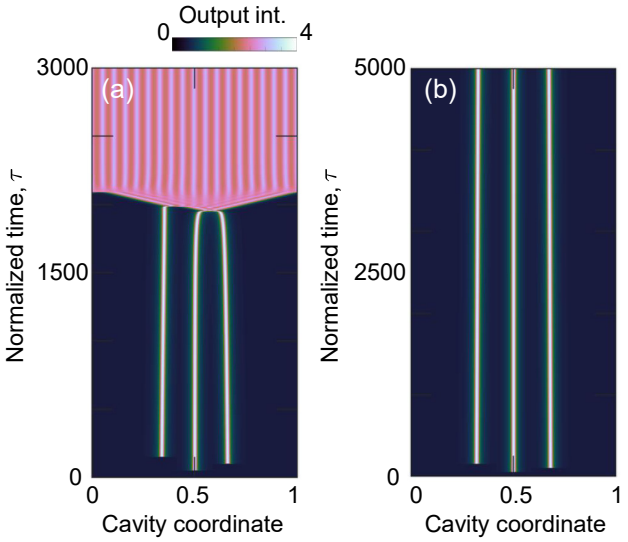

Figure 8: $Y = 7$. (a) A pulse is injected too close ($D = 0.16$) to an existing cavity soliton (CS); the emission profile is destabilized towards rolls. (b) The distance between the CS and two adjacent pulses is now $D = 0.17$, three independent CSs emerge at regime.

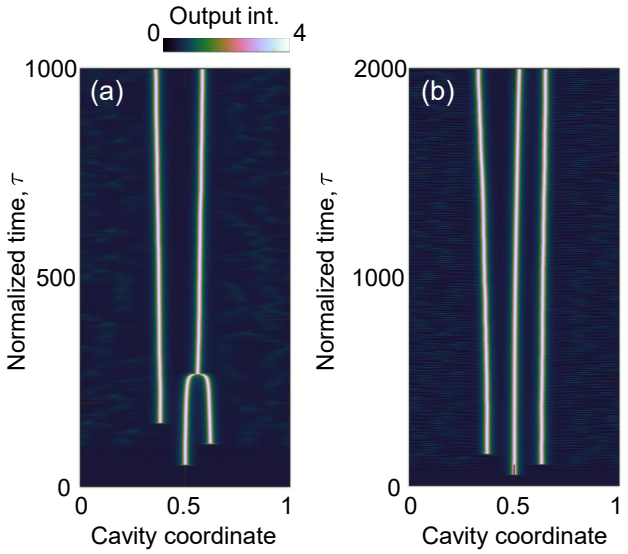

Figure 9: (a) Cavity solitons (CSs) merge into a single CS for $Y = 6.6$. (b) For $Y = 6.4$ CSs do not merge at reported minimum distances, but they push/pull each other modifying their separation.

We first considered the case $Y = 7$ where the HSS is stable and the system is close to the lower turning point. The initial state is precisely the HSS, then three short pulses of amplitude $\epsilon = 0.3$ are added to Y in sequence after $\tau = 50$, 100 and 150 at cavity locations $\eta_0/\eta_{\max} = 0.5$, $0.5 + D$ and $0.5 - D$, respectively. As it turns out, the system is quite sensitive to the perturbation of an existing CS, caused by the turn-on process of another one, so that when CSs are excited too closely, they interact attractively and the merger causes the emission profile to switch to the rolls (Figure 8(a)). For $D \geq 0.17$ instead the CSs are correctly written and reach a regime (Figure 8(b)).

We point out that the CS in presence of a stable homogeneous background does not exhibit oscillating tails, see Figure 2c in the study by Columbo et al. [14]. This excludes the possibility that bounded states can be formed among CS in this instance due to tail interaction [33, 34]. Although long-range CS interaction was predicted in CS without tails [35, 36] or much beyond the tail ringing range [37], a thorough analysis of CS interaction mechanisms exceeds the scopes of the present work and will be studied in the future.

Reducing Y brings the system farther from the turning point and makes it less sensitive to CS interactions. We may interpret in this sense the evidence that, when CSs are excited below the critical distance, they merge but no rolls switching occurs (Figure 9(a)). Also accordingly, we found that for $Y = 6.8$, 6.7, 6.6 interaction, distances to obtain independent CSs are $D = 0.16$, 0.14, 0.13, respectively. We could observe that for $Y < 6.8$, the background fluctuations grow more and more relevant and they seem to 'convey' perturbations across CS locations. This means that CSs do not merge at reported minimum distances, but they push/pull each other modifying their separation as in Figure 9(b), and more markedly as Y decreases. No such pushing occurs for e.g. $Y = 7$.

It is interesting that in this regime, where the CS background is unstable, the profile of the CS tails cannot be estimated altogether because it is drowned in the background fluctuations. Thus, again, interactions cannot be interpreted in terms of tail interaction. Similar CS behaviour (attraction/repulsion) in planar devices with irregular background emission was reported by Rahmani Anbardan et al. [38].

We remark that, in agreement with what was determined for transverse 2D CSs [32], the critical distances are on the order of the spatial modulation of the Turing rolls emerging from the MI which was estimated at $\lambda_{roll} = 0.117$ [14].

5.3 CS manipulation

It is well known that dissipative structures are sensitive to gradients appearing in control parameters, which set them in motion allowing the information they carry to be transported and redistributed (see the review [39] and references quoted therein). Indeed, other mechanisms can set CS in motion, such as thermal effects [40], higher-order dispersion and inhomogeneities [41, 42], coherent optical

feedback [43] or delayed response [44], but we will focus here on the basic external control paths that a driven laser provides, namely, we apply gradients in the input field and in the pump current. Experiments with 2D, transverse CSs measured soliton drift speeds at 470 m/s in broad-area vertical cavity surface emitting lasers [45] when a field gradient was provided. This property is confirmed in the case of our devices, where we could observe CS drift longitudinally inside the cavity, under the influence of input field gradients. To this purpose, the input profile the external field F_I was modified as follows:

$$\overline{F}_I(\tau,\eta) = F_I[1+\epsilon\mathcal{M}(\eta-\eta_s)], \tag{8}$$

where ϵ measures the field modulation strength, $\mathcal{M}$ is a suitable function of the cavity coordinate η and η_s is a possible spatial shift, to displace the field profile with respect to the cavity centre. Note that the value of ϵ must be small enough to ensure that, throughout the whole cavity, the field never exceeds the ranges where the CS is stable.

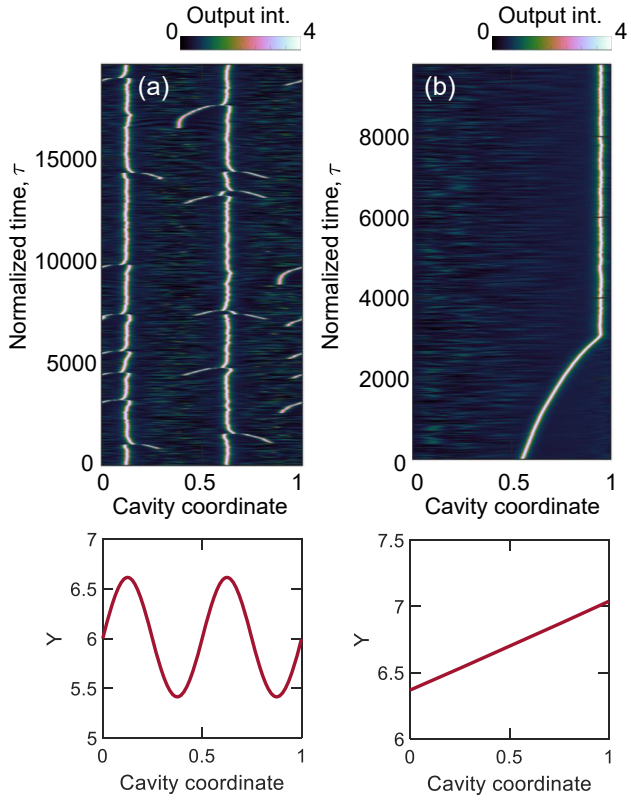

Figure 10: (a) Upper panel: cavity solitons (CSs) are spontaneously excited inside the cavity and follow the positive gradient of the field profile, being trapped at regime on the local maxima. Lower panel: intensity profile of the input field across the cavity. ($Y = 6.0$) (b) Upper panel: a CS follows the linear gradient with non-uniform velocity. Lower panel: intensity profile of the input field across the cavity ($Y = 6.7$).

We initially aimed to confirm that CS follow positive gradients and are trapped in the maxima of the input field profile, to this purpose we chose $\epsilon = 0.05$, $\mathcal{M} = \sin(4\pi\eta/\eta_{\max})$ so to have two maxima inside the cavity, and we selected $Y = 6$ which corresponds to a regime where the lower branch is unstable and CS are spontaneously created due to the spatio-temporal fluctuations of the background. As expected, all CS are attracted towards the maxima, as shown in Figure 10(a).

To estimate the drift speed of the CS a more regular field modulation was chosen by taking $\mathcal{M} = \eta - \eta_s$. The simulations reported in Figure 10(b) show that the CS follows the gradient and stops in the proximity of the cavity edge, where the input field abruptly changes by ϵ when η changes from 0 to 1 (which are equivalent points in a ring cavity due to the boundary conditions). The output field shows a negative hump on the left side of the cavity whose negative gradient, felt by the CS across the ring boundary, may balance the positive input field gradient, as shown in Figure 11. Surprisingly, the soliton does not move at constant speed as opposed to what was found for 2D CSs in semiconductor devices, where their velocity was shown proportional to the neutral mode corresponding to translation symmetries, which in turn is associated to the field gradient [31]. The reason for this discrepancy will be the object of future investigations.

While a precise evaluation of the CS speed is beyond the scopes of this work, by varying the parameter ϵ and shifting the gradient by adopting different values of η_s we could estimate the average CS speed $V_{CS} = \frac{\Delta\eta}{\Delta\tau}$ on the order

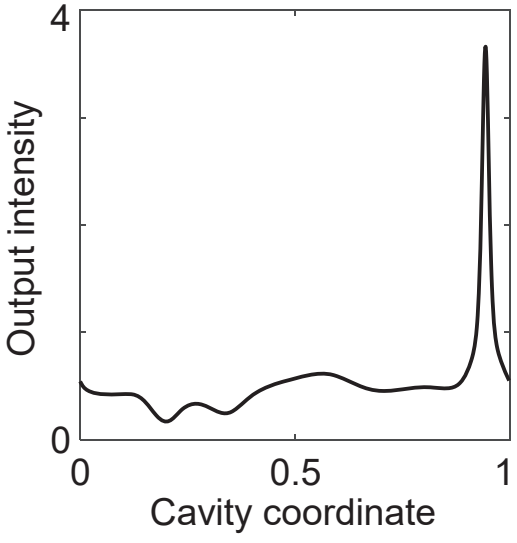

Figure 11: The output intensity profile relative to the simulation of Figure 10(b) shows that a negative hump is present on the left of the cavity, producing an effective negative gradient.

of $0.5 \times 10^{-3}\,\epsilon$. Considering a 3-mm cavity and the unit of time τ equal to 0.5 ns, this translates to $V_{CS} \approx 3 \times 10^{3}\,\epsilon$ m/s.

While coupling a modulated input field into the ring cavity might pose technical problems, assuming a modulated pump profile is less challenging, given recent RF techniques capable of modulating a microresonator at the beatnote frequency [46]. We wished to assess the behaviour of a CS when a weak modulation of the pump appearing in Eq. (1) is modelled by assuming $\mu = \mu_0 + \mu_1(\eta)$. By following the scaling leading to Eq. (3), one finds the form

$$\frac{\partial F(\tau,\eta)}{\partial \tau} = F_I + \gamma[1+\xi(\eta) - i\theta - i\Delta\xi(\eta)]F - (1-i\Delta)|F|^2F + (1+iG)\frac{\partial^2 F}{\partial \eta^2}, \quad (9)$$

with $\xi(\eta) = \mu_1(\eta)/(\mu_0 - 1)$. We simulated such a spatial dependent term in our model selecting $\xi(\eta) = \xi_0 \sin(2\pi\eta/\eta_{max} - \pi)$ and we could verify that the CS shifts at constant speed and is not pinned in modulation extrema as Figure 12 shows. In addition, reversing the sign of the modulated pump component changes the sign of the CS velocity leaving its speed unchanged. Although speed evaluation is left for future work, we checked that speed may be varied with the modulation amplitude ξ_0 and possibly by choosing different modulation shapes.

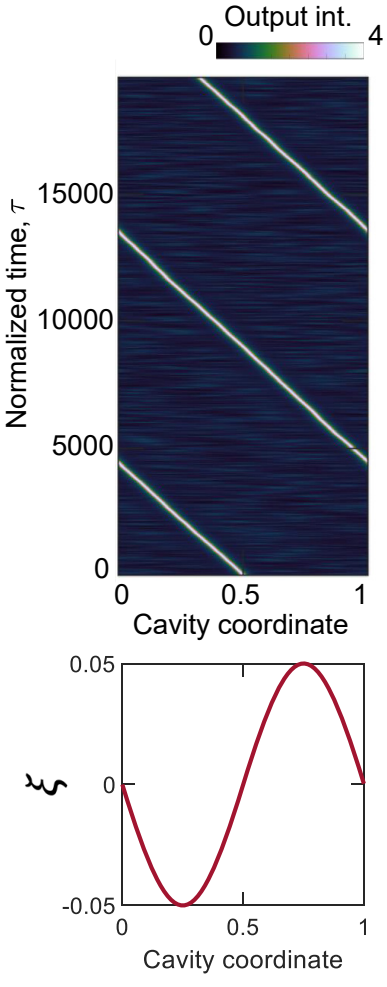

Figure 12: A cavity soliton (CS) drifts continuously along the cavity in presence of pump modulation, plotted in the lower panel. Here $Y = 6.7$ and $\xi_0 = 0.05$.

We remark that, in accordance with our preliminary evidence, a pump modulation will cause the CS to change its position inside the cavity, i.e. to change its propagation speed, and thus will influence the roundtrip time, although this change is quite modest. A regular change of the modulation, e.g. an AC modulation of the pump, may instead continuously change the lag between successive passages of the CS at the exit mirror, inducing a bit FM and possibly changing the associated comb composition.

6 Conclusion and perspectives

In this work, we presented the study of the HSS (or continuous wave) instabilities and the localized pattern dynamics occurring in a unidirectional ring QCL, driven by an external field. By exploiting a previously assessed model based on a generalized LLE, we could identify the character of the HSS emission curve as well as the oscillatory and modulational instabilities which affect it and determine the dynamical scenery the system will exhibit.

Our analysis allows considering the influence of all the main features affecting the semiconductor laser dynamics, such as the LEF, the forcing amplitude and detuning, the bias and, possibly, the GVD. The analyses allowed us to establish credible and promising candidates for the observation of localized structures of different classes, which exhibit remarkable interest for applications, relative to both optical comb formation and ultrashort pulse generation.

Extended simulation streams allowed characterizing different emission regimes, such as Turing rolls, but most importantly, evidencing the formation of two distinct classes of optical solitons. The first one, the PS, is associated to a chiral charge and connects the QCL to other classes of previously studied semiconductor lasers. The second, the cavity soliton, is a well-known pivotal element in optical comb formation (e.g. in Kerr microresonator) and information encoding, which we can now confirm in this new class of forefront, chip-scale and ultrafast lasers.

We confirm CS viability for applications, by showing independent addressing as well as all their salient features such as pair interaction and controlled drift. Further research will certainly lead us to address the possibility to

exploit suitably assembled collections of solitary structures to tailor the shape of the associated spectral comb. We will also investigate in this respect the effects of shaping and modulating in time the external field and the bias current.

Finally the outcomes of this work will be a valuable guideline to assess operating regimes and layout configurations for ongoing experimental activities.

Author contribution: All the authors have accepted responsibility for the entire content of this submitted manuscript and approved submission.
Research funding: None declared.
Conflict of interest statement: The authors declare no conflicts of interest regarding this article.

References

[1] T. Udem, R. Holzwarth, and T. W. Hänsch, "Optical frequency metrology," *Nature*, vol. 416, pp. 233–237, 2002.
[2] D. J. Jones, S. A. Diddams, J. K. Ranka, et al., "Carrier-envelope phase control of femtosecond mode-locked lasers and direct optical frequency synthesis," *Science*, vol. 288, p. 635, 2000.
[3] P. Del'Haye, A. Schliesser, O. Arcizet, T. Wilken, R. Holzwarth, and T. J. Kippenberg, "Optical frequency comb generation from a monolithic microresonator," *Nature*, vol. 450, pp. 1214–1217, 2007.
[4] T. J. Kippenberg, R. Holzwarth, and S. A. Diddams, "Microresonator-based optical frequency combs," *Science*, vol. 332, 2011, https://doi.org/10.1126/science.1193968.
[5] Chembo, and Y. K. Kerr, "Optical frequency combs: theory, applications and perspectives," *Nanophotonics*, vol. 5, pp. 214–230, 2016.
[6] L. A. Lugiato, F. Prati, M. L. Gorodetsky, and T. J. Kippenberg, "From the Lugiato-Lefever equation to microresonator-based soliton Kerr frequency combs," *Philos. T. R. Soc. A*, vol. 376, p. 20180113, 2018.
[7] A. Hugi, G. Villares, S. Blaser, H. Liu, and J. Faist, "Mid-infrared frequency comb based on a quantum cascade laser," *Nature*, vol. 492, pp. 229–233, 2012.
[8] D. Burghoff, T.-Y. Kao, N. Han, et al., "Terahertz laser frequency combs," *Nat. Photonics*, vol. 8, pp. 462–467, 2014.
[9] Q. Lu, M. Razeghi, S. Slivken, et al., "High power frequency comb based on mid-infrared quantum cascade laser at λ ~9μm," *Appl. Phys. Lett.*, vol. 106, p. 051105, 2015.
[10] J. Faist, G. Villares, G. Scalari, et al., "Quantum cascade laser frequency combs," *Nanophotonics*, vol. 5, pp. 272–291, 2016.
[11] T. Mansuripur, C. Vernet, P. Chevalier, et al., "Single-mode instability in standing-wave lasers: the quantum cascade laser as a self-pumped parametric oscillator," *Phys. Rev. A*, vol. 94, p. 063807, 2016.
[12] L. Columbo, S. Barbieri, C. Sirtori, and M. Brambilla, "Dynamics of a broad-band quantum cascade laser: from chaos to coherent dynamics and mode-locking," *Opt. Express*, vol. 26, pp. 2829–2847, 2018.
[13] M. Piccardo, B. Schwarz, D. Kazakov, et al., "Frequency combs induced by phase turbulence," *Nature*, vol. 582, pp. 360–364, 2020.
[14] L. Columbo, M. Piccardo, F. Prati, et al., "Unifying frequency combs in active and passive cavities: temporal solitons in externally-driven ring lasers," arXiv:20 07.07533 [physics.optics].
[15] L. A. Lugiato, and R. Lefever, "Spatial dissipative structures in passive optical systems," *Phys. Rev. Lett.*, vol. 58, pp. 2209–2211, 1987.
[16] L. A. Lugiato, C. Oldano, and L. M. Narducci, "Cooperative frequency locking and stationary spatial structures in lasers," *J. Opt. Soc. Am. B*, vol. 5, pp. 879–888, 1988.
[17] N. Akhmediev and A. Ankiewicz, *Dissipative Solitons. Lecture Notes in Physics*, Berlin, Heidelberg, Springer, 2005.
[18] T. J. Kippenberg, A. L. Gaeta, M. Lipson, and M. L. Gorodetsky, "Dissipative Kerr solitons in optical microresonators," *Science*, vol. 361, 2018, https://doi.org/10.1126/science.aan8083.
[19] C. Henry, "Theory of the linewidth of semiconductor lasers," *IEEE J. Quantum Electron.*, vol. 18, pp. 259–264, 1982.
[20] I. Aranson, and L. Kramer, "The world of the complex Ginzburg-Landau equation," *Rev. Mod. Phys.*, vol. 74, pp. 99–143, 2002.
[21] D. Burghoff, "Frequency-modulated combs as phase solitons," arXiv:2006.12397, 2020.
[22] M. Tlidi, P. Mandel, and R. Lefever, "Localized structures and localized patterns in optical bistability," *Phys. Rev. Lett.*, vol. 73, pp. 640–643, 1994.
[23] S. Wieczorek, B. Krauskopf, T. Simpson, and D. Lenstra, "The dynamical complexity of optically injected semiconductor lasers," *Phys. Rep.*, vol. 416, pp. 1–128, 2005.
[24] L. Lugiato, F. Prati, and M. Brambilla, *Nonlinear Optical Systems*, Cambridge, UK, Cambridge University Press, 2015.
[25] H. Chaté, A. Pikovsky, and O. Rudzick, "Forcing oscillatory media: phase kinks vs. synchronization," *Physica D*, vol. 131, pp. 17–30, 1999.
[26] F. Gustave, L. Columbo, G. Tissoni, et al., "Dissipative phase solitons in semiconductor lasers," *Phys. Rev. Lett.*, vol. 115, p. 043902, 2015.
[27] F. Gustave, L. Columbo, G. Tissoni, et al., "Phase solitons and domain dynamics in an optically injected semiconductor laser," *Phys. Rev. A*, vol. 93, p. 063824, 2016.
[28] F. Gustave, L. Columbo, G. Tissoni, et al., "Formation of phase soliton complexes in an optically injected semiconductor laser," *Eur. Phys. J. D*, vol. 71, p. 154, 2017.
[29] T. Ackemann, W. Firth, and G. Oppo, "Fundamentals and applications of spatial dissipative solitons in photonic devices," *Adv. At. Mol. Opt. Phys.*, vol. 57, pp. 323–421, 2009.
[30] I. Cristiani, R. Tediosi, L. Tartara, and V. Degiorgio, "Dispersive wave generation by solitons in microstructured optical fibers," *Opt. Express*, vol. 12, pp. 124–135, 2004.
[31] T. Maggipinto, M. Brambilla, G. K. Harkness, and W. J. Firth, "Cavity solitons in semiconductor microresonators: existence, stability, and dynamical properties," *Phys. Rev. E*, vol. 62, pp. 8726–8739, 2000.
[32] M. Brambilla, L. A. Lugiato, and M. Stefani, "Interaction and control of optical localized structures," *Europhys. Lett.*, vol. 34, pp. 109–114, 1996.
[33] A. Scroggie, W. Firth, G. S. McDonald, et al., "Pattern formation in a passive Kerr cavity," *Chaos Solitons Fract.*, vol. 4, pp. 1323–1354, 1994.
[34] A. Vladimirov, J. McSloy, D. Skryabin, and W. Firth, "Two-dimensional clusters of solitary structures in driven optical cavities," *Phys. Rev. E*, vol. 65, p. 11, 2002.

[35] H. Vahed, R. Kheradmand, H. Tajalli, et al., "Phase-mediated long-range interactions of cavity solitons in a semiconductor laser with a saturable absorber," *Phys. Rev. A*, vol. 84, pp. 063814-1–063814-6, 2011.
[36] S. Rahmani Anbardan, C. Rimoldi, R. Kheradmand, G. Tissoni, and F. Prati, "Exponentially decaying interaction potential of cavity solitons," *Phys. Rev. E*, vol. 97, p. 032208, 2018.
[37] Y. Wang, F. Leo, J. Fatome, et al., "Universal mechanism for the binding of temporal cavity solitons," *Optica*, vol. 4, pp. 855–863, 2017.
[38] S. Rahmani Anbardan, C. Rimoldi, R. Kheradmand, G. Tissoni, and F. Prati, "Interaction of cavity solitons on an unstable background," *Phys. Rev. E*, vol. 101, p. 042210, 2020.
[39] W. J. Firth, in *Soliton-driven Photonics, NATO Science Series (Series II: Mathematics, Physics and Chemistry)*, A. D. Boardman and A. P. Sukhorukov, Eds., Dordrecht, Springer, 2001.
[40] A. Scroggie, J. McSloy, and W. Firth, "Self-propelled cavity solitons in semiconductor microcavities," *Phys. Rev. E*, vol. 66, p. 036607, 2002.
[41] P. Parra-Rivas, D. Gomila, M. Matías, P. Colet, and L. Gelens, "Effects of inhomogeneities and drift on the dynamics of temporal solitons in fiber cavities and microresonators," *Opt. Express*, vol. 22, pp. 30943–30954, 2014.
[42] M. Liu, L. Wang, Q. Sun, et al., "Influences of high-order dispersion on temporal and spectral properties of microcavity solitons," *Opt. Express*, vol. 26, pp. 16477–16487, 2018.
[43] M. Tlidi, and K. Panajotov, "Two-dimensional dissipative rogue waves due to timedelayed feedback in cavity nonlinear optics," *Chaos*, vol. 27, p. 013119, 2017.
[44] M. G. Clerc, S. Coulibaly, and M. Tlidi, "Time-delayed nonlocal response inducing traveling temporal localized structures," *Phys. Rev. Res.*, vol. 2, p. 013024, 2020.
[45] X. Hachair, S. Barland, L. Furfaro, et al., "Cavity solitons in broad-area vertical-cavity surface-emitting lasers below threshold," *Phys. Rev. A*, vol. 69, no. 4, p. 043817, 2004.
[46] H. Li, P. Laffaille, D. Gacemi, et al., "Dynamics of ultra-broadband terahertz quantum cascade lasers for comb operation," *Opt. Express*, vol. 23, pp. 33270–33294, 2015.

Supplementary Material: The online version of this article offers supplementary material (https://doi.org/10.1515/nanoph-2020-0409).